

# Upconversion Plasmonic Lasing from an Organolead Trihalide Perovskite Nanocrystal with Low Threshold

Yu-Jung Lu,\* Teng Lam Shen, Kang-Ning Peng, Pi-Ju Cheng, Shu-Wei Chang, Ming-Yen Lu, Chih Wei Chu, Tzung-Fang Guo, and Harry A. Atwater\*

Cite This: <https://dx.doi.org/10.1021/acsp Photonics.0c01586>

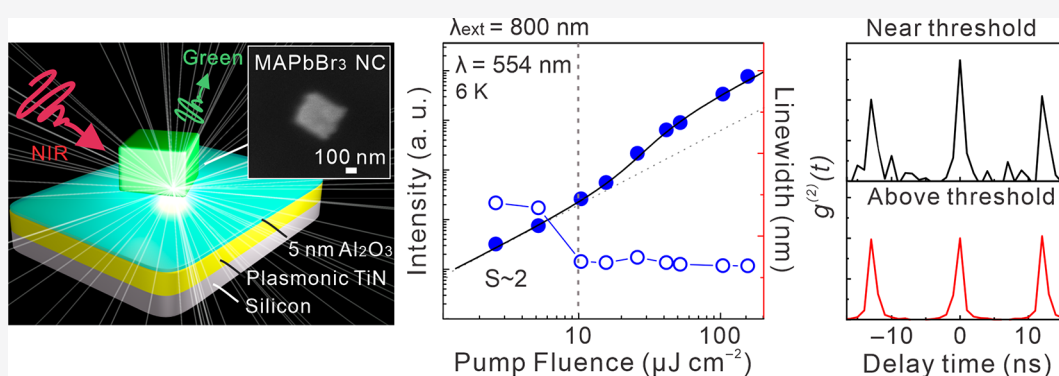
Read Online

ACCESS |

Metrics & More

Article Recommendations

Supporting Information



**ABSTRACT:** The understanding of nonlinear light–matter interactions at the nanoscale has fueled worldwide interest in upconversion emission for imaging, lasing, and sensing. Upconversion lasers with anti-Stokes-type emission with various designs have been reported. However, reducing the volume and lasing threshold of such lasers to the nanoscale level is a fundamental photonics challenge. Here, we demonstrate that the upconversion efficiency can be improved by exploiting single-mode upconversion lasing from a single organo-lead halide perovskite nanocrystal in a resonance-adjustable plasmonic nanocavity. This upconversion plasmonic nanolaser has a very low lasing threshold ( $10 \mu\text{J cm}^{-2}$ ) and a calculated ultrasmall mode volume ( $\sim 0.06 \lambda^3$ ) at 6 K. To provide the unique feature for lasing action, a temporal coherence signature of the upconversion plasmonic nanolasing was determined by measuring the second-order correlation function. The localized-electromagnetic-field confinement can be tailored in titanium nitride resonance-adjustable nanocavities, enhancing the pump-photon absorption and upconverted photon emission rate to achieve lasing. The proof-of-concept results significantly expand the performance of upconversion nanolasers, which are useful in applications such as on-chip, coherent, nonlinear optics, information processing, data storage, and sensing.

**KEYWORDS:** titanium nitride, lead halide perovskites, plasmonics, nanolasers, upconversion lasing, ENZ

A central challenge for nanolaser design is to achieve the small mode volume and device footprint needed to enable high density integration, low power consumption, and fast switching times.<sup>1,2</sup> In response to this challenge, plasmonic nanolasers and surface plasmon amplification by stimulated emission of radiation (SPASER)<sup>3–6</sup> have been demonstrated using various designs.<sup>5,7–24</sup> However, ultracompact upconversion emission via multiphoton pumped lasing has been more challenging<sup>25–29</sup> due to the required high material performance and control of optical modes and gain characteristics, which is a key issue for multiphoton pumped lasers based on rare-earth-doped upconversion nanoparticles (UCNPs).<sup>28,29</sup> To date, methylammonium lead trihalide perovskites<sup>30–34</sup> (MAPbX<sub>3</sub>, X = Cl, Br, I) have received considerable attention as gain media for lasers, mainly with the aim of achieving an economic and tunable diode laser.<sup>30,32</sup> The solution processability, long carrier diffusion lengths, wavelength tunability, large exciton binding

energy, high optical gain coefficients ( $>10^4 \text{ cm}^{-1}$ ),<sup>31</sup> and promising two-photon absorption characteristics favor the use of halide perovskite gain media in lasers. However, reducing the volume of perovskite-based lasers<sup>18,23,25,30–39</sup> to the nanoscale for small mode volume lasing from a single nanoemitter is a challenge in nanophotonics.<sup>1,2</sup>

## RESULTS AND DISCUSSION

Here, we demonstrate upconversion lasing from a single perovskite nanoemitter enabled by the strong local plasmonic

Received: October 12, 2020

field from a MAPbBr<sub>3</sub> perovskite nanocrystal (PNC) integrated with an Al<sub>2</sub>O<sub>3</sub>/TiN (5 nm/80 nm) plasmonic cavity (Figure 1a).

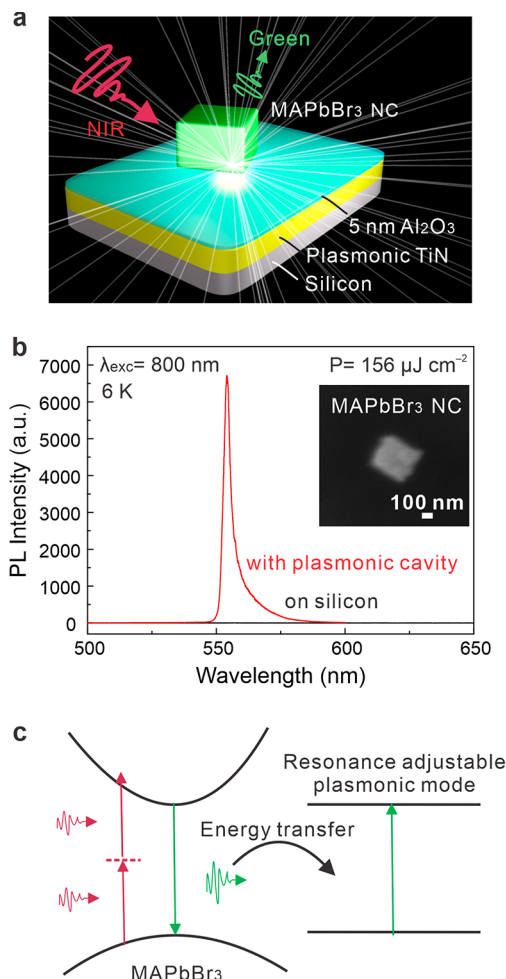


**Figure 1.** Upconversion plasmonic nanolaser. (a) Schematic of the lasing device. A MAPbBr<sub>3</sub> perovskite nanocrystal (PNC) is placed on an 80 nm plasmonic TiN film with a 5 nm Al<sub>2</sub>O<sub>3</sub> separation layer inserted between them. (b) Comparison between the emission spectra of single PNC with particular size on the Al<sub>2</sub>O<sub>3</sub>/TiN plasmonic platform and on silicon under excitation by a near-infrared (NIR) pulsed laser. The plasmonic cavity enhances the upconversion luminescence by 4500-fold. (c) Working process of the upconversion plasmonic nanolaser. The NIR pump laser excites electron–hole pairs in the PNC through two-photon absorption (red arrow). The radiative recombination of relaxed electron–hole pairs emits energy quanta at visible wavelengths (green arrow), which are then transferred to modes of the plasmonic cavity with adjustable plasmon resonance (black arrows). The strength of the localized electromagnetic field alters the energy transfer efficiency.

Critically, we find that the use of a plasmonic cavity results in a significant enhancement of the nonlinear optical response,<sup>28,40</sup> enabling low-threshold upconversion lasing. Solution-processed MAPbBr<sub>3</sub> PNCs were chosen as the gain media due to their strong photoluminescence and remarkable insensitivity to surface defects, which is important for the high surface-to-volume ratio needed for nanolaser gain media (see Methods for the detailed sample fabrication),<sup>41–43</sup> such as that in single-crystalline nanocrystals with edge lengths in the range of 100–500 nm. Under two-photon optical excitation at 800 nm via 100 fs Ti:sapphire laser pulses with an 80 MHz repetition rate, single-

mode upconversion lasing action was successfully demonstrated. We observed enhancement of both the effective absorption cross section and the energy transfer efficiency arising from the localized electromagnetic (EM) field overlapping with the PNC, which is difficult to achieve with PNCs alone due to the poorer optical confinement in small-footprint dielectric cavities than in plasmonic nanocavities. As shown in Figure 1b, the upconversion luminescence from a single PNC with particular size (an edge length of 300 nm and a height of 100 nm) is increased 4500-fold in a plasmonic nanocavity. The SEM image shows the measured single PNC on silicon. The working principle of the upconversion plasmonic nanolaser is shown in Figure 1c: near-infrared pump photons excite electron–hole pairs in the PNC through two-photon absorption. The radiative recombination of relaxed electron–hole pairs emits photons at visible wavelengths that couple to plasmonic modes of the tunable TiN plasmonic nanocavity, for which the energy transfer efficiency between the photons and localized surface plasmons strongly depends on the strength of the cavity mode.

Distinct from other conventional plasmonic lasers using silver, gold, or aluminum as the plasmonic medium, we employed an atomically smooth plasmonic TiN film as an alternative plasmonic platform. Important for lasing nanocavities, TiN is a durable high-temperature material whose melting point is three times higher than that of gold or other traditional plasmonic materials,<sup>44</sup> and its plasmonic properties can be tailored by the growth conditions.<sup>45</sup> Here, plasmonic TiN was sputter-deposited onto a silicon (Si) substrate using radio frequency (RF) magnetron sputtering at 800 °C (see Tables S1 and S2). To achieve upconversion lasing, both the optical gain and system loss must be carefully controlled. The atomically smooth TiN surface reduces the scattering losses that would otherwise hamper the achievement of lasing action. As shown in Figure 2a, atomic force microscopy (AFM) reveals that the 80 nm thick plasmonic TiN film has an average surface roughness of less than 0.5 nm, suggesting a low scattering loss. Notably, the imaginary part of the TiN film dielectric permittivity indicates that the loss is comparable to that of gold, which is commonly utilized as a plasmonic material. Additionally, plasmonic TiN is robust to high-temperature damage to the device due to the small negative magnitude of the real part of its permittivity, which is different from gold. The epsilon-near-zero (ENZ) wavelength of TiN is adjustable by varying the growth conditions, as shown in Figure 2. The material properties of TiN can be adjusted to yield either an optically dielectric phase ( $\text{Re}(\epsilon) > 0$ ) or an optically plasmonic phase ( $\text{Re}(\epsilon) < 0$ ) at a given wavelength (see Figure 2b). Distinct from the lower carrier concentration exhibited by doped oxides and other semiconductors whose ENZ wavelengths lie in the near- or mid-infrared wavelength range,<sup>46,47</sup> TiN exhibits an ENZ wavelength in the visible range.<sup>48–51</sup> The ability to adjust the ENZ wavelength of TiN films in the visible range plays a crucial role in the observation of plasmonic upconversion lasing.

We designed an upconversion plasmonic nanolaser with adjustable resonance by optimizing the coupling strength between the plasmonic nanocavity and the methylammonium lead trihalide perovskite nanoemitter. MAPbBr<sub>3</sub> PNCs were chosen as a gain medium because of their strong photoluminescence (PL) due to the remarkable reduction of surface defects<sup>41–43</sup> and their large two-photon absorption coefficient.<sup>52</sup> For comparison, we measured the upconversion PL from both a single MAPbBr<sub>3</sub> PNC and a single CsPbBr<sub>3</sub> PNC on silicon, and only observed two-photon PL from the single MAPbBr<sub>3</sub> PNC at

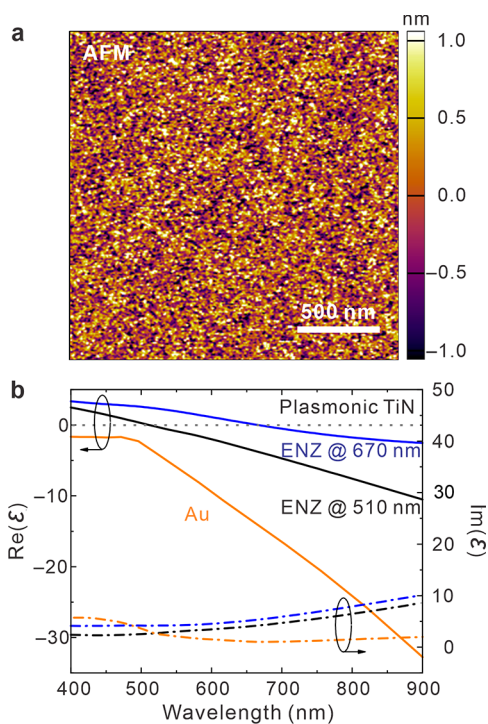


**Figure 2.** Titanium nitride plasmonic platform with adjustable plasmon resonance. (a) Atomic force microscopy (AFM) image of an atomically smooth TiN film (80 nm thick) with an average surface roughness of 0.5 nm. (b) Real (solid line) and imaginary (dash-dotted line) parts of the dielectric permittivities obtained from two TiN films via spectroscopic ellipsometry. The two films have epsilon-near-zero (ENZ) wavelengths at 510 and 670 nm, respectively. The permittivity of gold, which is a commonly used plasmonic material, is also included for comparison (Johnson and Christy).<sup>60</sup>

6 K (see Figure S1). This is due to the reported two-photon absorption coefficient of MAPbBr<sub>3</sub> (8.6 cm/GW) being 2 orders

of magnitude higher than that of CsPbBr<sub>3</sub> (0.085 cm/GW),<sup>52,53</sup> thus, increasing the upconversion efficiency. The optical properties of MAPbBr<sub>3</sub> PNCs were characterized by ultra-violet–visible and PL spectroscopy (see Figure S2). In addition, we measured the temperature-dependent PL spectra from a PNC on a Si substrate from room temperature down to 6 K (Figure 3a). We observed that the emission peaks red-shifted from 516 to 543 nm with decreasing temperature. Different from the trend for typical semiconductors, the unusual redshift of the PL in lead perovskites with decreasing temperature has been attributed to a phase transition.<sup>54,55</sup> The phase of the perovskite can be identified as the orthorhombic, tetragonal or cubic phase in different temperature ranges,<sup>54,55</sup> as shown in Figure 3a. These results reveal that the PNC is in a cubic phase at room temperature, which is in agreement with the following crystal structure characterization. Moreover, a significant PL enhancement from the MAPbBr<sub>3</sub> PNC at cryogenic temperature was observed, and the redshift of the PL in perovskites with decreasing temperature plays a key role in this study (see Figure S3). To ensure that the operation conditions favor lasing in the plasmonic mode, we inspected the PL of the PNC, which is also an indicator of the optical gain profile, and found that it overlapped well with the designed plasmon resonance mode profile at 6 K.

To characterize the crystallinity of the PNC, we investigated its crystal structure by transmission electron microscopy (TEM) at room temperature. The low-magnification bright-field (BF) TEM image, corresponding to a selected area diffraction (SAD) pattern and the high-resolution (HR) TEM images shown in Figure 3b–d, confirms the cubic morphology and the single-crystalline nature of the PNC. Figure 3e displays the atomic model of MAPbBr<sub>3</sub>, which has a cubic structure with the space group of *Pm* $\bar{3}$ *m*. The atomic arrangements of the MAPbBr<sub>3</sub> cube along the [11–1] zone are further visualized based on the annular bright-field (ABF) scanning TEM image in Figure 3f. Thus, the high crystallinity and the well-passivated surface that

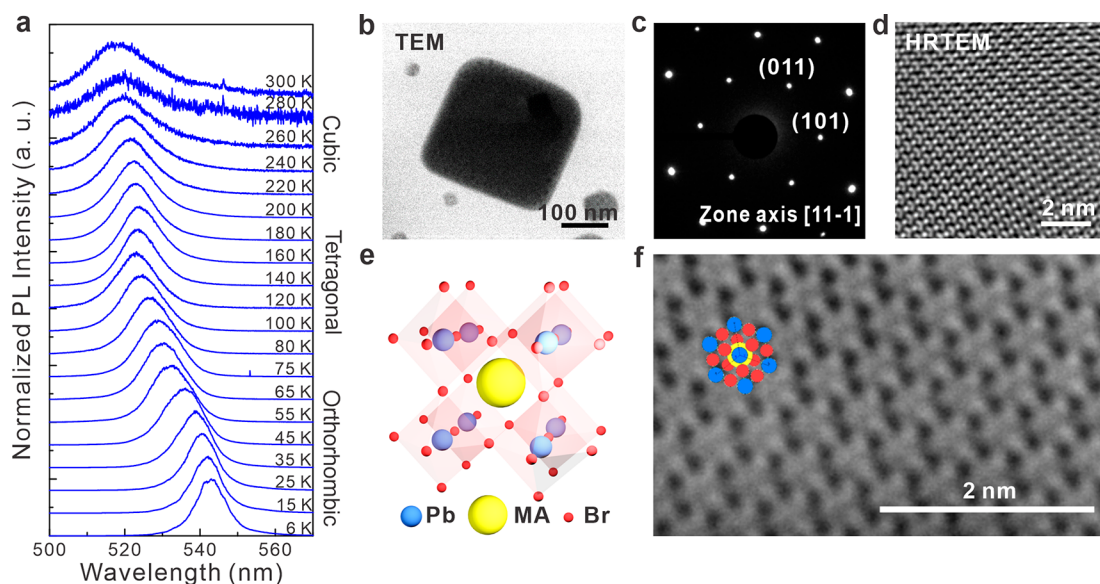


**Figure 3.** Material characteristics of a MAPbBr<sub>3</sub> perovskite nanocrystal (PNC). (a) Temperature-dependent photoluminescence (PL) spectra of a PNC on silicon measured from room temperature down to 6 K under one-photon excitations. The emission peak redshifts from 516 to 543 nm with decreasing temperature due to the phase transition from cubic to orthorhombic. (b–d) Structural analyses of a single-crystalline PNC based on transmission electron microscopy (TEM), including a bright-field TEM image, the corresponding selected area diffraction pattern, and a high-resolution (HR) TEM image. (e, f) Annular bright-field scanning TEM image reflecting the cubic structure of MAPbBr<sub>3</sub>.

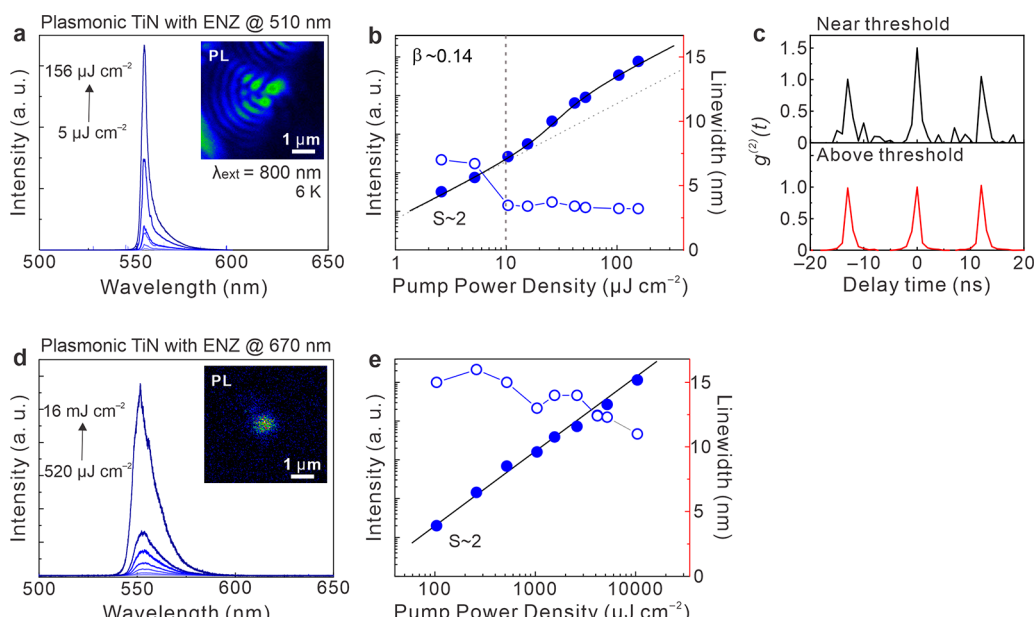


**Figure 4.** Upconversion plasmonic nanolasing characterization at 6 K. (a) Upconversion emission spectra of a MAPbBr<sub>3</sub> perovskite nanocrystal (PNC) on top of an Al<sub>2</sub>O<sub>3</sub>/TiN (S/80 nm) plasmonic platform with an epsilon-near-zero (ENZ) wavelength of TiN at 510 nm at different pump levels (on resonance). The photoluminescence (PL) mapping reflects the coherence feature of the nanolasing. Color indicates emission intensity. (b) Optical intensity and line width vs pump fluence at the lasing peak (554 nm) for the nanolasing source in (a) with a lasing threshold of 10  $\mu\text{J cm}^{-2}$ . (c) Temporal coherence signature of the plasmonic upconversion nanolaser obtained by second-order photon correlation function measurements. (d) Upconversion emission spectra of a PNC on the same type of plasmonic cavity with an ENZ wavelength of TiN at 670 nm at different pump levels (off resonance). The PL mapping exhibits characteristics of spontaneous emission. (e) Optical intensity and line width vs pump fluence for the photon source in (d). The absence of sharp line-width narrowing indicates that the device persists as an incoherent photon emitter.

eliminates most of the quenching pathways are even more critical for lasing than for PL.

Plasmonic upconversion nanolasing was achieved when the optical gain profile overlapped well with the plasmonic resonance. We demonstrated single-mode upconversion lasing from a single PNC on top of 5 nm Al<sub>2</sub>O<sub>3</sub>-covered plasmonic TiN with an ENZ wavelength at 510 nm (see Figure 2b) as a resonance-adjustable plasmonic nanocavity (510 nm ENZ device). A thin dielectric layer of Al<sub>2</sub>O<sub>3</sub> was deposited by atomic layer deposition (ALD) between the PNC and the plasmonic TiN substrate to avoid PL quenching.<sup>7,14</sup> As shown in Figure 4a, the single-mode lasing peak was centered at 554 nm with a line width of 3 nm, which was pumped by a near-infrared Ti:sapphire pulsed laser at 800 nm through two-photon absorption. Lasing was achieved when the emission peak from the PNC was spectrally aligned with the plasmonic resonance mode. In calculating the cavity mode, we note that the PNC in this particular device has an edge length of 300 nm and a height of 100 nm. The inset in Figure 4a shows the PL mapping of the nanolasing source. The emission intensity and line width of the upconversion laser versus the pump fluence are shown in Figure 4b. The light-in light-out ( $L-L$ ) curve at the lasing peak (554 nm) on the log-log scale and the corresponding emission line width narrowing behavior show a very low upconversion lasing threshold of 10  $\mu\text{J cm}^{-2}$  at 6 K with ultrasmall footprint, which is relatively small in the literature-reported value of upconversion perovskite lasing (see Table S3). However, it is not easy to make a fair comparison of lasing threshold because some of the reported lasers operated at room temperature. The lasing signature can be determined from the nonlinear “S”-shape of the  $L-L$  curve. Below the lasing threshold, we obtained a slope in the  $L-L$  plot of 2, which represents the feature of spontaneous emission. In addition, the line width of the emission spectra

decreased from  $>7$  nm (below the threshold) to 3 nm (well above the threshold) when lasing occurred. To estimate the threshold gain of the plasmonic mode, we solved for the eigenmodes for successively increasing values of the imaginary part of the permittivity of the perovskite using a three-dimensional finite-element method. The predicted threshold gain that compensates for the absorption and radiation losses is approximately 3382  $\text{cm}^{-1}$  (see Figure S4). The lead trihalide perovskite has been reported to possess a large gain coefficient ( $>10^4 \text{ cm}^{-1}$ ),<sup>31</sup> which is capable of providing sufficient optical gain to overcome the system loss to reach the lasing condition. In addition, the calculated cavity mode has a very small mode volume of  $\sim 0.06 \lambda^3$  (see Figure S4). Moreover, the spontaneous emission coupling factor,  $\beta$ , is estimated as 0.14 based on the fitting of the light-in light-out plot. This modest coupling factor indicates that there is room for improving the coupling efficiency between the spontaneous emission and plasmonic modes in our upconversion nanolaser (see Note S5 in the Supporting Information). The spontaneous emission coupling factor  $\beta$  can be improved by increasing the coupling efficiency of the spontaneous emission to the lasing mode. One possible way to increase the  $\beta$  value is to design a structure that has a lasing mode with extensive overlap in the PNC, which increases the coupling efficiency. Note that a higher  $\beta$  value indicates a higher coupling efficiency, which decreases the lasing threshold of the device. We believe that by optimizing the plasmonic properties of the TiN film or replacing the optical gain medium by using a MAPbI<sub>3</sub> PNC with efficient red emission, a lasing with high  $\beta$  value can be achieved, thereby enhancing the coupling strength between the optical gain medium and cavity. We obtained measurements of the second-order photon correlation function,<sup>14,56,57</sup>  $g^{(2)}(t)$ , to provide a unique temporal coherence signature for lasing action (see Figures S5 and S6). As presented in Figure 4c, the photon

correlation function  $g^{(2)}(t = 0)$  under an excitation power near the lasing threshold shows a thermal bunched behavior, representing amplified spontaneous emission. We observed that  $g^{(2)}(t = 0)$  approaches unity under an excitation power above the lasing threshold, which represents the temporal coherence signature of lasing. Note that the lasing peak intensity remained constant and without a wavelength shift for more than 4 h.

Additionally, we measured the upconversion emission spectrum from a MAPbBr<sub>3</sub> PNC on the same type of plasmonic nanocavity but with an ENZ wavelength of TiN at 670 nm (see Figures 2b and 4d). In this case (the PNC on 670 nm ENZ device), the optical gain is spectrally misaligned with the plasmonic resonance, resulting in spontaneous emission only, even if the pump fluence is 3 orders of magnitude stronger than that used in Figure 4a. The PL mapping image of this device only shows the characteristics of spontaneous emission. Moreover, the emission intensity versus pump fluence exhibits a slope of 2 on a log–log scale, representing the feature of spontaneous emission. The line widths at various pump levels are mostly greater than 10 nm and are characteristically broadband, as expected for spontaneous emission behavior. In comparison, the line widths of the PNC on Si at various pump levels are approximately 6–7 nm, which represent the spontaneous emission from a single PNC (see Figure S1). A spectral broadening behavior can be observed in Figure 4e; the emission line widths at various pump levels are greater than 10 nm due to the placement of the emitter near the TiN, which behaved as a lossy dielectric. Note that the line width of the PNC on the 510 nm ENZ device at the pump power below threshold is approximately 7.5 nm (see Figure 4b), which is very close to the line widths of the PNC on silicon. Compared to the line width of the PNC on the 670 nm ENZ device, that on the 510 nm ENZ device is decreased at the pump power below threshold, indicating that the system loss of PNC on the 510 nm ENZ device is less than that on the 670 nm ENZ device. As a result, the lasing action can only be observed in the case of PNC on the 510 nm ENZ device, which has higher coupling efficiency than the other device. Given that the pump fluences in Figure 4d,e are 3 orders of magnitude stronger than those in Figure 4a,b, these results indicate the strong role that adjustable plasmonic resonance plays in the functioning of our upconversion plasmonic nanolaser. Given that the pump fluences in Figure 4d,e are 3 orders of magnitude stronger than those in Figure 4a,b, these results reflect the strong role that an adjustable plasmonic resonance plays in our upconversion plasmonic nanolaser.

Both the two-photon absorption and the emission rate are important for approaching lasing action. By integrating a single PNC with a plasmonic cavity, we can potentially enhance the localized EM field, which boosts the upconversion emission rate owing to an enhancement of the absorption cross section through the local field.<sup>28,29</sup> If  $E_0$  and  $E(\mathbf{r}_0)$  are the incident and local electric fields at  $\mathbf{r}_0$ , respectively, then the two-photon absorption cross section is enhanced by a factor of  $(|E(\mathbf{r}_0)|/|E_0|)^4$ . In Figure 5a, the calculated distribution of  $|E|^4$  of the EM field at a wavelength of 800 nm represents the two-photon pumping rate. In this case of the PNC situated on top of 5 nm Al<sub>2</sub>O<sub>3</sub>-covered plasmonic TiN with an ENZ wavelength of TiN at 510 nm (Figure 5a), the strong field localized in the dielectric gap induces nonlinear photon absorption therein, resulting in a plasmonic-enhanced two-photon absorption cross section. This can be interpreted as resulting from the strong confinement of

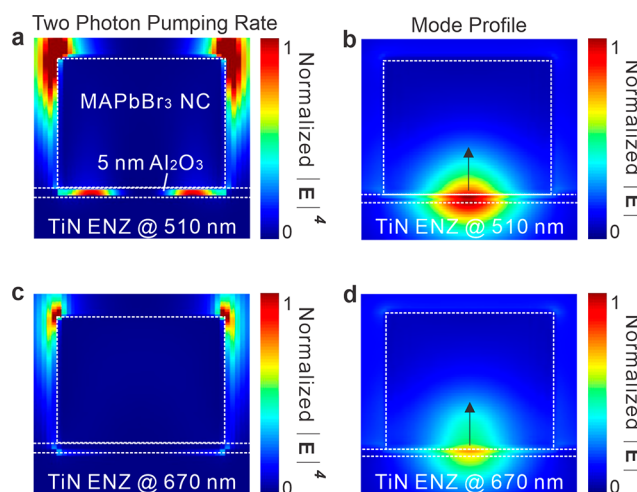


**Figure 5.** Working principle of upconversion plasmonic lasing with adjustable plasmon resonance. (a) Calculated distribution of  $|E|^4$  at 800 nm, the two-photon pumping rate, for a perovskite nanocrystal placed on the Al<sub>2</sub>O<sub>3</sub>/TiN (5/80 nm) plasmonic platform with an epsilon-near-zero (ENZ) wavelength of TiN at 510 nm. The strong local electromagnetic field in the dielectric gap that penetrates into the perovskite nanocrystal induces nonlinear absorption therein. (b) Corresponding mode profile at the emission wavelength showing strong optical confinement in the gap and prominent mode overlap with the perovskite. (c) Distribution of  $|E|^4$  at 800 nm for the counterpart plasmonic cavity with an ENZ wavelength of TiN at 670 nm. Almost no light confinement of the pump field can be observed. (d) Corresponding mode profile at the emission wavelength showing weak optical confinement in the gap and insignificant mode overlap with the perovskite.

the pump field in the dielectric gap leading to a localized surface plasmon resonance,<sup>7,9,10,14,15,20,21</sup> thus, enhancing the nonlinear light–matter interaction. Moreover, the calculated mode profile at the emission wavelength (see Figure 5b) reveals that the field is also tightly confined in the dielectric gap, indicating prominent overlap between the plasmonic cavity mode and PNC. The strong mode overlap in the PNC results in an increase in the energy transfer rate between the photons and surface plasmons (see Figure 1c), enabling lasing action to be reached. We also calculated the EM field distribution of  $|E|^4$  at 800 nm for the complementary plasmonic cavity with an ENZ wavelength of TiN at 670 nm. In this case, the optical gain profile is spectrally misaligned with the plasmon resonance. Thus, almost no optical confinement of the near-infrared pump field can be observed in the dielectric gap (see Figure 5c). In addition, the calculated cavity mode profile at the emission wavelength shows a weakly confined EM field in the dielectric gap and overlaps poorly with the PNC (see Figure 5d). This agrees with our experimental results, as shown in Figure 4d,e.

To perform an appropriate comparison, we also measured the upconversion emission from a PNC on an Al<sub>2</sub>O<sub>3</sub>/gold (5 nm/100 nm) plasmonic nanocavity. However, no signal could be detected, and the measurement was limited by the severe thermal damage incurred at high pump powers. These results can be attributed to the significant negative real part of the permittivity in gold, which makes approaching the lasing condition more difficult for the cavity due to local heating. These results indicate that the ohmic loss of the TiN film is less than that of gold. Another factor for plasmonic upconversion lasing should also be taken into account: the perovskite single crystal exhibits the characteristic of photon recycling.<sup>58</sup>

Therefore, by integrating a PNC with a plasmonic cavity, photons can be reabsorbed and re-emitted by the perovskite gain medium without being lost via irreversible heat dissipation, making the lasing threshold more accessible in the presence of a metal. In the present work, we characterized 6 upconversion nanolaser devices. Although the upconversion plasmonic lasers in this work were operated at cryogenic temperatures, this proof-of-concept study on adjustable plasmonic mode profiles and adjustable pump rates is extensible to other types of emitters. We believe that, by optimizing the plasmonic properties of the TiN film or replacing the gain medium using a MAPbI<sub>3</sub> PNC with efficient red emission to enhance the coupling efficiency of the spontaneous emission to the lasing mode, a room-temperature plasmonic upconversion nanolasing can be realized.

## CONCLUSION

In summary, we have proposed and demonstrated a new type of plasmonic nanolaser for realizing upconversion lasing that consists of thermostable TiN as a promising resonance-adjustable plasmonic platform and a bottom-up MAPbBr<sub>3</sub> PNC as a nonlinear optical gain medium, for which it is an excellent candidate. We observed single-mode emission from the upconversion plasmonic nanolaser with an ultralow upconversion lasing threshold of 10  $\mu\text{J cm}^{-2}$ , which is at least 3 orders of magnitude smaller than the threshold for the reference sample (a PNC on silicon). By measuring the second-order correlation function, a temporal coherence signature of the plasmonic upconversion nanolasing was determined. The working principle is that, with the low-loss plasmonic cavity, the strong localized EM field-induced dual enhancement of both the two-photon pumping rate and the emission rate enables upconversion lasing action from a single perovskite nanoemitter. The plasmonic cavity enhances the upconversion luminescence by 4500-fold. In addition, the small device footprint with a calculated ultrasmall mode volume ( $\sim 0.06 \lambda^3$ ) allows for high density integration, low power consumption and a fast switching time.<sup>1,2</sup> Thus, our finding opens a new pathway toward on-chip coherent nonlinear optics with potential applications in imaging, data storage, quantum information technology, integrated nanophotonics, and optical communication.

## METHODS

**Sample Fabrication.** We synthesized single-crystalline MAPbBr<sub>3</sub> PNCs using a solution-based process in a nitrogen-filled glovebox (with oxygen and moisture levels <1 ppm).<sup>59</sup> The MAPbBr<sub>3</sub> PNCs were synthesized by doping MAPbBr<sub>3</sub> film with chlorine. Methylammonium bromide (0.153 g), lead bromide (0.4815 g), and choline chloride (0.036 g) were mixed in a dimethyl sulfoxide (DMSO) solution (1.07 mL) and stirred for 12 h under a N<sub>2</sub> atmosphere. The precursor solution was spin-coated atop glass substrates using a consecutive two-step spin-coating process at 500 rpm (for 7 s) and 4000 rpm (for 70 s). During the spin-coating process, 250  $\mu\text{L}$  of chloroform was dripped on the surface of the precursor film at 50 s. Organo-lead trihalide perovskite MAPbBr<sub>3</sub> nanocrystals were successfully synthesized on the glass substrate after annealing at 70 °C for 10 min. After that, the nanocrystals with sizes ranging from 100 to 500 nm were suspended in a hexane solution using a sonic bath for 10 min and then dispersed onto Al<sub>2</sub>O<sub>3</sub>-capped TiN film by drop-casting diluted suspension solutions of the nanocrystals. The Al<sub>2</sub>O<sub>3</sub> thin film was deposited by atomic layer deposition (ALD).

**Optical Measurement.** The upconversion lasing measurements were collected at a temperature of 6 K on a closed-cycle cryogenic system (Attodry 800, attocube) equipped with a confocal laser scanning microscope system and a spectrometer (SR-500i, Andor) consisting of a monochromator and a thermoelectrically cooled CCD camera. The resolution of the spectrometer is 0.06 nm. A femtosecond Ti:sapphire laser (Spectra-Physics) that provides 100 fs, 800 nm pulses at a repetition rate of 80 MHz was used to optically pump the sample. A 100 $\times$  objective lens (0.82 NA; attocube) was used to focus the pulsed laser to a small spot with a diameter of approximately 1  $\mu\text{m}$ . To filter out the excitation laser signal, a 750 nm short-pass filter was placed in front of the spectrometer. For the measurements of the second-order correlation function,  $g^{(2)}(t)$ , a Hanbury Brown-Twiss (HB-T) setup with a time resolution of  $\sim 500$  ps was used. The emission signal was fed into two Si single-photon-counting avalanche photodiodes by using a 50/50 beamsplitter. Then, the second-order correlation function was observed via quantum correlation analysis software (QuCou, PicoQuant).

**Simulation.** The optical field distributions were calculated using the finite-difference time-domain (FDTD; Lumerical Solutions, Inc.) method. We solved the eigenmodes and the predicted threshold gain of the plasmonic nanocavity with the three-dimensional finite-element method (COMSOL eigenfrequency solver). Detailed simulation parameters are shown in the Supporting Information.

## ASSOCIATED CONTENT

### Supporting Information

The Supporting Information is available free of charge at <https://pubs.acs.org/doi/10.1021/acsp Photonics.0c01586>.

Detailed discussion of the sample fabrication, experimental detail, and fitting model; Characterization of plasmonic TiN films; Optical properties of perovskite nanocrystals; Table of the reported two-photon-pumped lasers; Theoretical analysis of the lasing threshold; Extraction of the spontaneous-emission coupling factor; Temporal coherence signature obtained by the second order correlation function measurements (PDF)

## AUTHOR INFORMATION

### Corresponding Authors

**Yu-Jung Lu** – Research Center for Applied Sciences, Academia Sinica, Taipei 11529, Taiwan; Thomas J. Watson Laboratories of Applied Physics, California Institute of Technology, Pasadena, California 91125, United States; Department of Physics, National Taiwan University, Taipei 10617, Taiwan; [orcid.org/0000-0002-3932-653X](https://orcid.org/0000-0002-3932-653X); Email: [yujunglu@gate.sinica.edu.tw](mailto:yujunglu@gate.sinica.edu.tw)

**Harry A. Atwater** – Thomas J. Watson Laboratories of Applied Physics, California Institute of Technology, Pasadena, California 91125, United States; [orcid.org/0000-0001-9435-0201](https://orcid.org/0000-0001-9435-0201); Email: [haa@caltech.edu](mailto:haa@caltech.edu)

### Authors

**Teng Lam Shen** – Research Center for Applied Sciences, Academia Sinica, Taipei 11529, Taiwan; Department of Photonics, National Cheng Kung University, Tainan 701, Taiwan

**Kang-Ning Peng** – Research Center for Applied Sciences, Academia Sinica, Taipei 11529, Taiwan

Pi-Ju Cheng – Research Center for Applied Sciences, Academia Sinica, Taipei 11529, Taiwan

Shu-Wei Chang – Research Center for Applied Sciences, Academia Sinica, Taipei 11529, Taiwan

Ming-Yen Lu – Department of Materials Science and Engineering, National Tsing-Hua University, Hsinchu 30013, Taiwan; [orcid.org/0000-0003-1788-1425](https://orcid.org/0000-0003-1788-1425)

Chih Wei Chu – Research Center for Applied Sciences, Academia Sinica, Taipei 11529, Taiwan; [orcid.org/0000-0003-0979-1729](https://orcid.org/0000-0003-0979-1729)

Tzung-Fang Guo – Department of Photonics, National Cheng Kung University, Tainan 701, Taiwan

Complete contact information is available at:

<https://pubs.acs.org/10.1021/acsp Photonics.0c01586>

### Author Contributions

Y.J.L. proposed the original idea, developed the theoretical aspects, and performed all experiments, calculations, and data analysis. Y.J.L., P.J.C., and S.W.C. carried out the simulations. T.L.S. and K.N.P. fabricated the perovskite samples, performed the optical measurements, and helped in discussion. M.Y.L. carried out the TEM analyses. C.W.C., T.F.G., S.W.C., and H.A.A. contributed to the discussion and revised the manuscript. Y.J.L. organized the project and wrote the paper. All authors discussed the results and commented on the manuscript.

### Notes

The authors declare no competing financial interest.

### ACKNOWLEDGMENTS

We thank Prof. Mikhail A. Noginov, Prof. Shangjr Gwo and Dr. Ruzan Sokhoyan for useful suggestions. The authors would like to thank Wen-Hui Cheng, Jing-Shun Huang, Cora Went, Wei-Hsiang Lin, Anya Mitskovets, and Meng-Ju Yu for useful discussions. We also acknowledge use of spectroscopic ellipsometry supported by Prof. Yia-Chung Chang. We acknowledge financial support from the Ministry of Science and Technology, Taiwan (Grant No. MOST-106-2112-M-001-036-MY3 (Y.J.L.); MOST-109-2112-M-001-043-MY3 (Y.J.L.); MOST-108-2221-E-001-018-MY3(S.W.C.); MOST 108-2113-M-006-005-MY3 (T.F.G.); MOST-109-2636-E-007-017 (M.Y.L.)) and Academia Sinica (Grant No. AS-CDA-108-M08 (Y.J.L.)), and also by the “Photonics at Thermodynamic Limits” Energy Frontier Research Center funded by the U.S. Department of Energy, Office of Science, Office of Basic Energy Sciences under Award Number DE-SC0019140 (H.A.A.).

### REFERENCES

- (1) Hill, M. T.; Gather, M. C. Advances in Small Lasers. *Nat. Photonics* **2014**, *8*, 908.
- (2) Ma, R.-M.; Oulton, R. F. Applications of Nanolasers. *Nat. Nanotechnol.* **2019**, *14*, 12–22.
- (3) Bergman, D. J.; Stockman, M. I. Surface Plasmon Amplification by Stimulated Emission of Radiation: Quantum Generation of Coherent Surface Plasmons in Nanosystems. *Phys. Rev. Lett.* **2003**, *90*, 027402.
- (4) Stockman, M. I. Spasers Explained. *Nat. Photonics* **2008**, *2*, 327.
- (5) Noginov, M. A.; Zhu, G.; Belgrave, A. M.; Bakker, R.; Shalae, V. M.; Narimanov, E. E.; Stout, S.; Herz, E.; Suteewong, T.; Wiesner, U. Demonstration of a Spaser-Based Nanolaser. *Nature* **2009**, *460*, 1110–1112.
- (6) Song, P.; Wang, J.-H.; Zhang, M.; Yang, F.; Lu, H.-J.; Kang, B.; Xu, J.-J.; Chen, H.-Y. Three-Level Spaser for Next-Generation Luminescent Nanoprobe. *Sci. Adv.* **2018**, *4*, eaat0292.

(7) Oulton, R. F.; Sorger, V. J.; Zentgraf, T.; Ma, R. M.; Gladden, C.; Dai, L.; Bartal, G.; Zhang, X. Plasmon Lasers at Deep Subwavelength Scale. *Nature* **2009**, *461*, 629–632.

(8) Nezhad, M. P.; Simic, A.; Bondarenko, O.; Slutsky, B.; Mizrahi, A.; Feng, L. A.; Lomakin, V.; Fainman, Y. Room-Temperature Sub-wavelength Metallo-Dielectric Lasers. *Nat. Photonics* **2010**, *4*, 395–399.

(9) Ma, R. M.; Oulton, R. F.; Sorger, V. J.; Bartal, G.; Zhang, X. Room-Temperature Sub-Diffraction-Limited Plasmon Laser by Total Internal Reflection. *Nat. Mater.* **2011**, *10*, 110–113.

(10) Lu, Y. J.; Kim, J.; Chen, H. Y.; Wu, C.; Dabidian, N.; Sanders, C. E.; Wang, C. Y.; Lu, M. Y.; Li, B. H.; Qiu, X.; Chang, W. H.; Chen, L. J.; Shvets, G.; Shih, C. K.; Gwo, S. Plasmonic Nanolaser Using Epitaxially Grown Silver Film. *Science* **2012**, *337*, 450–453.

(11) Suh, J. Y.; Kim, C. H.; Zhou, W.; Huntington, M. D.; Co, D. T.; Wasielewski, M. R.; Odom, T. W. Plasmonic Bowtie Nanolaser Arrays. *Nano Lett.* **2012**, *12*, 5769–5774.

(12) Khajavikhan, M.; Simic, A.; Katz, M.; Lee, J. H.; Slutsky, B.; Mizrahi, A.; Lomakin, V.; Fainman, Y. Thresholdless Nanoscale Coaxial Lasers. *Nature* **2012**, *482*, 204–207.

(13) Zhou, W.; Dridi, M.; Suh, J. Y.; Kim, C. H.; Co, D. T.; Wasielewski, M. R.; Schatz, G. C.; Odom, T. W. Lasing Action in Strongly Coupled Plasmonic Nanocavity Arrays. *Nat. Nanotechnol.* **2013**, *8*, 506–511.

(14) Lu, Y. J.; Wang, C. Y.; Kim, J.; Chen, H. Y.; Lu, M. Y.; Chen, Y. C.; Chang, W. H.; Chen, L. J.; Stockman, M. I.; Shih, C. K.; Gwo, S. All-Color Plasmonic Nanolasers with Ultralow Thresholds: Autotuning Mechanism for Single-Mode Lasing. *Nano Lett.* **2014**, *14*, 4381–4388.

(15) Zhang, Q.; Li, G.; Liu, X.; Qian, F.; Li, Y.; Sum, T. C.; Lieber, C. M.; Xiong, Q. A Room Temperature Low-Threshold Ultraviolet Plasmonic Nanolaser. *Nat. Commun.* **2014**, *5*, 4953.

(16) Yang, A.; Hoang, T. B.; Dridi, M.; Deeb, C.; Mikkelsen, M. H.; Schatz, G. C.; Odom, T. W. Real-Time Tunable Lasing from Plasmonic Nanocavity Arrays. *Nat. Commun.* **2015**, *6*, 6939.

(17) Ho, J.; Tatebayashi, J.; Sergent, S.; Fong, C. F.; Ota, Y.; Iwamoto, S.; Arakawa, Y. A Nanowire-Based Plasmonic Quantum Dot Laser. *Nano Lett.* **2016**, *16*, 2845–2850.

(18) Yu, H.; Ren, K.; Wu, Q.; Wang, J.; Lin, J.; Wang, Z.; Xu, J.; Oulton, R. F.; Qu, S.; Jin, P. Organic–Inorganic Perovskite Plasmonic Nanowire Lasers with a Low Threshold and a Good Thermal Stability. *Nanoscale* **2016**, *8*, 19536–19540.

(19) Galanzha, E. I.; Weingold, R.; Nedosekin, D. A.; Sarimollaoglu, M.; Nolan, J.; Harrington, W.; Kuchyanov, A. S.; Parkhomenko, R. G.; Watanabe, F.; Nima, Z.; Biris, A. S.; Plekhanov, A. I.; Stockman, M. I.; Zharov, V. P. Spaser as a Biological Probe. *Nat. Commun.* **2017**, *8*, 15528.

(20) Wang, S.; Wang, X. Y.; Li, B.; Chen, H. Z.; Wang, Y. L.; Dai, L.; Oulton, R. F.; Ma, R. M. Unusual Scaling Laws for Plasmonic Nanolasers Beyond the Diffraction Limit. *Nat. Commun.* **2017**, *8*, 1889.

(21) Wang, S.; Chen, H. Z.; Ma, R. M. High Performance Plasmonic Nanolasers with External Quantum Efficiency Exceeding 10. *Nano Lett.* **2018**, *18*, 7942–7948.

(22) Deeb, C.; Guo, Z.; Yang, A.; Huang, L.; Odom, T. W. Correlating Nanoscopic Energy Transfer and Far-Field Emission to Unravel Lasing Dynamics in Plasmonic Nanocavity Arrays. *Nano Lett.* **2018**, *18*, 1454–1459.

(23) Huang, C.; Sun, W.; Fan, Y.; Wang, Y.; Gao, Y.; Zhang, N.; Wang, K.; Liu, S.; Wang, S.; Xiao, S.; Song, Q. Formation of Lead Halide Perovskite Based Plasmonic Nanolasers and Nanolaser Arrays by Tailoring the Substrate. *ACS Nano* **2018**, *12*, 3865–3874.

(24) Lin, Y.; Wang, D.; Hu, J.; Liu, J.; Wang, W.; Guan, J.; Schaller, R. D.; Odom, T. W. Engineering Symmetry-Breaking Nanocrescent Arrays for Nanolasing. *Adv. Funct. Mater.* **2019**, *29*, 1904157.

(25) Xu, Y.; Chen, Q.; Zhang, C.; Wang, R.; Wu, H.; Zhang, X.; Xing, G.; Yu, W. W.; Wang, X.; Zhang, Y.; Xiao, M. Two-Photon-Pumped Perovskite Semiconductor Nanocrystal Lasers. *J. Am. Chem. Soc.* **2016**, *138*, 3761–3768.

(26) Xing, G. C.; Liao, Y. L.; Wu, X. Y.; Chakraborty, S.; Liu, X. F.; Yeow, E. K. L.; Chan, Y.; Sum, T. C. Ultralow-Threshold Two-Photon Pumped Amplified Spontaneous Emission and Lasing from Seeded

CdSe/CdS Nanorod Heterostructures. *ACS Nano* **2012**, *6*, 10835–10844.

(27) Zhang, W.; Peng, L.; Liu, J.; Tang, A.; Hu, J. S.; Yao, J.; Zhao, Y. S. Controlling the Cavity Structures of Two-Photon-Pumped Perovskite Microlasers. *Adv. Mater.* **2016**, *28*, 4040–4046.

(28) Dong, J.; Gao, W.; Han, Q.; Wang, Y.; Qi, J.; Yan, X.; Sun, M. Plasmon-Enhanced Upconversion Photoluminescence: Mechanism and Application. *Rev. in Phys.* **2019**, *4*, 100026.

(29) Fernandez-Bravo, A.; Wang, D.; Barnard, E. S.; Teitelboim, A.; Tajon, C.; Guan, J.; Schatz, G. C.; Cohen, B. E.; Chan, E. M.; Schuck, P. J.; Odom, T. W. Ultralow-Threshold, Continuous-Wave Upconverting Lasing from Subwavelength Plasmons. *Nat. Mater.* **2019**, *18*, 1172–1176.

(30) Zhu, H.; Fu, Y.; Meng, F.; Wu, X.; Gong, Z.; Ding, Q.; Gustafsson, M. V.; Trinh, M. T.; Jin, S.; Zhu, X. Y. Lead Halide Perovskite Nanowire Lasers with Low Lasing Thresholds and High Quality Factors. *Nat. Mater.* **2015**, *14*, 636–642.

(31) Sutherland, B. R.; Sargent, E. H. Perovskite Photonic Sources. *Nat. Photonics* **2016**, *10*, 295.

(32) Zhang, Q.; Su, R.; Du, W.; Liu, X.; Zhao, L.; Ha, S. T.; Xiong, Q. Advances in Small Perovskite-Based Lasers. *Small Methods* **2017**, *1*, 1700163.

(33) Wang, K.; Wang, S.; Xiao, S.; Song, Q. Recent Advances in Perovskite Micro- and Nanolasers. *Adv. Opt. Mater.* **2018**, *6*, 1800278.

(34) Lin, C.-H.; Li, T.-Y.; Zhang, J.; Chiao, Z.-Y.; Wei, P.-C.; Fu, H.-C.; Hu, L.; Yu, M.-J.; Ahmed, G. H.; Guan, X.; Ho, C.-H.; Wu, T.; Ooi, B. S.; Mohammed, O. F.; Lu, Y.-J.; Fang, X.; He, J.-H. Designed Growth and Patterning of Perovskite Nanowires for Lasing and Wide Color Gamut Phosphors with Long-Term Stability. *Nano Energy* **2020**, *73*, 104801.

(35) Zhang, Q.; Ha, S. T.; Liu, X.; Sum, T. C.; Xiong, Q. Room-Temperature Near-Infrared High-Q Perovskite Whispering-Gallery Planar Nanolasers. *Nano Lett.* **2014**, *14*, 5995–6001.

(36) Zhang, Q.; Su, R.; Liu, X.; Xing, J.; Sum, T. C.; Xiong, Q. High-Quality Whispering-Gallery-Mode Lasing from Cesium Lead Halide Perovskite Nanoplatelets. *Adv. Funct. Mater.* **2016**, *26*, 6238–6245.

(37) Huang, C.; Wang, K.; Yang, Z.; Jiang, L.; Liu, R.; Su, R.; Zhou, Z.-K.; Wang, X. Up-Conversion Perovskite Nanolaser with Single Mode and Low Threshold. *J. Phys. Chem. C* **2017**, *121*, 10071–10077.

(38) Tiguntseva, E.; Koshelev, K.; Furasova, A.; Tonkaev, P.; Mikhailovskii, V.; Ushakova, E. V.; Baranov, D. G.; Shegai, T.; Zakhidov, A. A.; Kivshar, Y.; Makarov, S. V. Room-Temperature Lasing from Mie-Resonant Nonplasmonic Nanoparticles. *ACS Nano* **2020**, *14*, 8149–8156.

(39) Liu, Z.; Yang, J.; Du, J.; Hu, Z.; Shi, T.; Zhang, Z.; Liu, Y.; Tang, X.; Leng, Y.; Li, R. Robust Subwavelength Single-Mode Perovskite Nanocuboid Laser. *ACS Nano* **2018**, *12*, 5923–5931.

(40) Nielsen, M. P.; Shi, X.; Dichtl, P.; Maier, S. A.; Oulton, R. F. Giant Nonlinear Response at a Plasmonic Nanofocus Drives Efficient Four-Wave Mixing. *Science* **2017**, *358*, 1179–1181.

(41) Zheng, X.; Chen, B.; Dai, J.; Fang, Y.; Bai, Y.; Lin, Y.; Wei, H.; Zeng, X. C.; Huang, J. Defect Passivation in Hybrid Perovskite Solar Cells Using Quaternary Ammonium Halide Anions And Cations. *Nat. Energy* **2017**, *2*, 17102.

(42) Abdi-Jalebi, M.; Andaji-Garmaroudi, Z.; Cacovich, S.; Stavrakas, C.; Philippe, B.; Richter, J. M.; Alsari, M.; Booker, E. P.; Hutter, E. M.; Pearson, A. J.; Lilliu, S.; Savenije, T. J.; Rensmo, H.; Divitini, G.; Ducati, C.; Friend, R. H.; Stranks, S. D. Maximizing and Stabilizing Luminescence from Halide Perovskites with Potassium Passivation. *Nature* **2018**, *555*, 497–501.

(43) Jiang, Q.; Zhao, Y.; Zhang, X.; Yang, X.; Chen, Y.; Chu, Z.; Ye, Q.; Li, X.; Yin, Z.; You, J. Surface Passivation of Perovskite Film for Efficient Solar Cells. *Nat. Photonics* **2019**, *13*, 460–466.

(44) Li, W.; Guler, U.; Kinsey, N.; Naik, G. V.; Boltasseva, A.; Guan, J.; Shalaev, V. M.; Kildishev, A. V. Refractory Plasmonics with Titanium Nitride: Broadband Metamaterial Absorber. *Adv. Mater.* **2014**, *26*, 7959–7965.

(45) Lu, Y.-J.; Sokhoyan, R.; Cheng, W.-H.; Kafaie Shirmanesh, G.; Davoyan, A. R.; Pala, R. A.; Thyagarajan, K.; Atwater, H. A.

Dynamically Controlled Purcell Enhancement of Visible Spontaneous Emission in a Gated Plasmonic Heterostructure. *Nat. Commun.* **2017**, *8*, 1631.

(46) Olivieri, A.; Chen, C.; Hassan, S.; Lisicka-Skrzek, E.; Tait, R. N.; Berini, P. Plasmonic Nanostructured Metal-Oxide-Semiconductor Reflection Modulators. *Nano Lett.* **2015**, *15*, 2304–2311.

(47) Huang, Y. W.; Lee, H. W. H.; Sokhoyan, R.; Pala, R. A.; Thyagarajan, K.; Han, S.; Tsai, D. P.; Atwater, H. A. Gate-Tunable Conducting Oxide Metasurfaces. *Nano Lett.* **2016**, *16*, 5319–5325.

(48) Boltasseva, A.; Atwater, H. A. Low-Loss Plasmonic Metamaterials. *Science* **2011**, *331*, 290–291.

(49) Naik, G. V.; Kim, J.; Boltasseva, A. Oxides and Nitrides as Alternative Plasmonic Materials in the Optical Range [Invited]. *Opt. Mater. Express* **2011**, *1*, 1090–1099.

(50) Naik, G. V.; Shalaev, V. M.; Boltasseva, A. Alternative Plasmonic Materials: Beyond Gold and Silver. *Adv. Mater.* **2013**, *25*, 3264–3294.

(51) Wang, Y.; Capretti, A.; Dal Negro, L. Wide Tuning of the Optical and Structural Properties of Alternative Plasmonic Materials. *Opt. Mater. Express* **2015**, *5*, 2415–2430.

(52) Walters, G.; Sutherland, B. R.; Hoogland, S.; Shi, D.; Comin, R.; Sellan, D. P.; Bakr, O. M.; Sargent, E. H. Two-Photon Absorption in Organometallic Bromide Perovskites. *ACS Nano* **2015**, *9*, 9340–9346.

(53) Wei, K.; Xu, Z.; Chen, R.; Zheng, X.; Cheng, X.; Jiang, T. Temperature-Dependent Excitonic Photoluminescence Excited by Two-Photon Absorption in Perovskite CsPbBr<sub>3</sub> Quantum Dots. *Opt. Lett.* **2016**, *41*, 3821–3824.

(54) Dar, M. I.; Jacopin, G.; Meloni, S.; Mattoni, A.; Arora, N.; Boziki, A.; Zakeeruddin, S. M.; Rothlisberger, U.; Grätzel, M. Origin of Unusual Bandgap Shift and Dual Emission in Organic-Inorganic Lead Halide Perovskites. *Sci. adv.* **2016**, *2*, e1601156.

(55) Meloni, S.; Palermo, G.; Ashari-Astani, N.; Grätzel, M.; Rothlisberger, U. Valence and Conduction Band Tuning in Halide Perovskites for Solar Cell Applications. *J. Mater. Chem. A* **2016**, *4*, 15997–16002.

(56) Strauf, S.; Hennessy, K.; Rakher, M. T.; Choi, Y. S.; Badolato, A.; Andreani, L. C.; Hu, E. L.; Petroff, P. M.; Bouwmeester, D. Self-Tuned Quantum Dot Gain in Photonic Crystal Lasers. *Phys. Rev. Lett.* **2006**, *96*, 127404.

(57) Wiersig, J.; Gies, C.; Jahnke, F.; Aßmann, M.; Berstermann, T.; Bayer, M.; Kistner, C.; Reitzenstein, S.; Schneider, C.; Höfling, S.; Forchel, A.; Kruse, C.; Kalden, J.; Hommel, D. Direct Observation of Correlations between Individual Photon Emission Events of a Microcavity Laser. *Nature* **2009**, *460*, 245–249.

(58) Fang, Y.; Wei, H.; Dong, Q.; Huang, J. Quantification of Re-Absorption and Re-Emission Processes to Determine Photon Recycling Efficiency in Perovskite Single Crystals. *Nat. Commun.* **2017**, *8*, 14417.

(59) Chih, Y.-K.; Wang, J.-C.; Yang, R.-T.; Liu, C.-C.; Chang, Y.-C.; Fu, Y.-S.; Lai, W.-C.; Chen, P.; Wen, T.-C.; Huang, Y.-C.; Tsao, C.-S.; Guo, T.-F. NiO<sub>x</sub> Electrode Interlayer and CH<sub>3</sub>NH<sub>2</sub>/CH<sub>3</sub>NH<sub>3</sub>PbBr<sub>3</sub> Interface Treatment to Markedly Advance Hybrid Perovskite-Based Light-Emitting Diodes. *Adv. Mater.* **2016**, *28*, 8687–8694.

(60) Johnson, P. B.; Christy, R. W. Optical Constants of the Noble Metals. *Phys. Rev. B* **1972**, *6*, 4370–4379.